

Twisted or Planar? Side-Chain Tailoring of Fluorene-Based Hole-Transport Materials for Efficient and Stable Perovskite Solar Cells

Rui Li, Maning Liu,* Sri Kasi Matta, Alaa Almasri, Jingshu Tian, Hongzhen Wang, Hannu Pekka Pasanen, Salvy P. Russo, Paola Vivo,* and Haichang Zhang*

The functionalization of small-molecule hole-transport materials (HTMs) heavily relies on the rational design of molecular geometry, which can optimize both intrinsic HTM properties and interfacial properties for realizing high-performance and stable lead halide perovskite solar cells (LHPSCs). Herein, two fluorene-based donor- π linker-donor HTMs are seen, FL01 and FL02, whose side chains are tailored with planar phenyl-carbazole groups and twisted triphenylamine groups, respectively. Benefiting from the high conformational flexibility of twisted side chains, the strong and oriented interaction via Pb—O bonding is well coordinated at the perovskite and FL02 interface, which favors the interfacial charge transfer as well as the protection of perovskite layer by effectively blocking or mitigating the diffusion of hygroscopic dopants toward the perovskite surface. Consequently, the performance of FL02 HTM-based n-i-p LHPSCs is significantly enhanced by achieving a power conversion efficiency of 17.8%, which is twice higher than that (8.6%) of FL01 HTM-based ones and comparable with the case (18.8%) of conventional spiro-OMeTAD HTM-based devices. More importantly, the FL02-based devices exhibit impressively high operation and storage stabilities with T80 and TS80 lifetimes of >98 h and \approx 270 days, respectively, which are among the longest lifespans for the type of hygroscopically doped LHPSCs.

1. Introduction

Within just one decade, the power conversion efficiency (PCE) of lead halide perovskite solar cells (LHPSCs) has been rapidly boosted up to recently certified 25.7%,^[1] which clearly highlights the considerable potential of LHPSCs as the most promising candidates for the third-generation solar cells. To date, most of high-performance (e.g., PCEs >20%) LHPSCs are constructed with an architecture of conventional n-i-p configuration,^[2–5] which comprises conductive glass/electron-transport material (ETM)/perovskite layer/hole-transport material (HTM)/metal electrode. Despite the achievement of high PCEs, the stability of LHPSCs is still not satisfactory, yet being a major barrier to their commercialization. The interfacial properties between perovskite layer and charge acceptors (i.e., ETM or HTM) are known to play a

R. Li, J. Tian, H. Wang, H. Zhang
Key Laboratory of Rubber-Plastics of Ministry of Education/Shandong Province (QUST)
School of Polymer Science and Engineering
Qingdao University of Science and Technology
Qingdao 266042, P. R. China
E-mail: haichangzhang@qust.edu.cn

M. Liu, A. Almasri, H. P. Pasanen, P. Vivo
Hybrid Solar Cells
Faculty of Engineering and Natural Sciences
Tampere University
FI-33014 Tampere, Finland
E-mail: maning.liu@tuni.fi; paola.vivo@tuni.fi


M. Liu
Centre for Analysis and Synthesis
Department of Chemistry
Lund University
22100 Lund, Sweden
E-mail: maning.liu@chem.lu.se

M. Liu
Wallenberg Initiative Materials Science for Sustainability
Department of Chemistry
Lund University
22100 Lund, Sweden

S. K. Matta, S. P. Russo
Australian Research Council Centre of Excellence in Exciton Science
School of Science
RMIT University
Melbourne, VIC 3000, Australia

S. K. Matta
JSPS International Research Fellow Center for Computational Sciences
University of Tsukuba
Tsukuba, Ibaraki 305-0006, Japan

A. Almasri
Department of Physics
Lappeenranta-Lahti University of Technology (LUT)
FI-53850 Lappeenranta, Finland

 The ORCID identification number(s) for the author(s) of this article can be found under <https://doi.org/10.1002/solr.202300367>.

© 2023 The Authors. Solar RRL published by Wiley-VCH GmbH. This is an open access article under the terms of the Creative Commons Attribution License, which permits use, distribution and reproduction in any medium, provided the original work is properly cited.

DOI: 10.1002/solr.202300367

key role in influencing both performance and stability of LHPSCs.^[6–8] For the n–i–p configuration, in most cases the interface between perovskite and organic HTM (e.g., 2,2',7,7'-tetrakis[*N,N*-di(4-methoxyphenyl)amino]-9,9'-spirobifluorene (Spiro-OMeTAD) and poly[bis(4-phenyl)(2,4,6-trimethylphenyl)amine] (PTAA)) is more sensitive or less robust compared to that between perovskite and inorganic ETM (e.g., TiO₂ or SnO₂). Moreover, the most widely used Spiro-OMeTAD HTM often requires a large thickness (≈150–300 nm) and the addition of hygroscopic dopants (e.g., lithium bis(trifluoromethanesulfonyl)imide (LiTFSI), and *tert*-butylpyridine (tBP)) to simultaneously achieve a dual-effect of sufficient hole extraction/collection by the metal electrode as well as high hole mobility within the HTM.^[4,9,10] Nevertheless, a thick Spiro-OMeTAD doped with hygroscopic additives can largely increase the fabrication cost and still cause the severe degradation of underneath perovskite layer within a short time. Numerous efforts have been made to replace the Spiro-OMeTAD layer in n–i–p LHPSCs by designing new organic small molecules with diverse functional groups, e.g., oxy-group,^[11] thiol-group,^[12] halogen bonding,^[13] and hydrogen bonding,^[14] which can effectively passivate the perovskite surface by interacting with uncoordinated Pb²⁺ or halide anions (e.g., I[−]) to enhance the device performance and stability.

Besides the integration of different functional groups within the HTMs, the interfacial functionalization is also very dependent on the geometry of the HTM molecules. A general design concept relies on the pursuit of higher planarity and longer conjugated orbits for enhancing the π – π stacking effect of the molecular skeleton, such as widely reported trianiline-based HTMs.^[15–17] However, high planarity can cause the blocking of conformational torsion of HTM molecules in space,^[18] which makes it difficult to evenly deposit the HTM on the surface of the perovskite layer, leading to the formation of more defects at the interface of perovskite and HTM. In addition, the HTM molecules with high planarity often have low solubility in nonpolar solvents (e.g., chlorobenzene or toluene),^[19] potentially resulting in the inhomogeneous HTM film morphology deposited on top of the perovskite layer. Thus, it is crucial to design a multifunctional small-molecule HTM in a trade-off way by balancing between planarity and twisting level for the molecular structure. Lin et al.^[20] designed one type of bimesitylene-based small molecules by tuning the twisted level of the skeleton with the insertion of benzene ring or thiophene group on the side chain. With the slightly twisted side chains in the HTM molecule, the as-fabricated n–i–p mesoporous LHPSCs achieved the highest PCE of 12.1%, which is comparable with the performance (PCE of 12.7%) of their reference cells based on Spiro-OMeTAD HTM, although the absolute PCE values are not as high as current benchmark (≈20%). Later, Yang et al.^[21] demonstrated a highly twisted small-molecule structure (i.e., XY1) by attaching four triphenylamine (TPA) substituents to a small thieno[2,3-*b*]thiophene core, leading to the increase in the solubility in organic solvents as well as in the glass transition temperature for acquiring good film morphology. The XY1 HTM-based devices exhibited much enhanced PCEs up to 18.8% and long lifespan with a 95% retainment of its initial PCE under continuous 1 sun illumination for 200 h, all of which are compared with the case (PCE of 16.3%) of

poly(3,4-ethylenedioxythiophene)poly(styrenesulfonate) (PEDOT:PSS)-based control devices but still in p–i–n inverted configuration. Therefore, low-cost organic small-molecule HTMs with well-balanced planar and twisted molecular structure to achieve high-performance and stable LHPSCs, particularly in n–i–p configuration, is still highly desirable.

In this work, we develop a small-molecule HTM, namely, FL02, with a donor– π -linker–donor (D– π -D) linear skeleton by deliberately choosing the building blocks to realize an optimized balance between planarity and torsion. Planar fluorene is selected as the π -linker because the fluorene-based molecules normally exhibit a characteristic of film thickness independent carrier mobility.^[22] Two substituted TPA groups are attached to the fluorene core as the side chains, which possess a feature of twisted conformation. As a comparison, the side chains of TPA groups are replaced with phenyl-carbazole (PCZ) groups for constructing the reference HTM FL01, which demonstrates the higher planarity at the molecular terminal compared to FL02. Density functional theory (DFT) calculations reveal that tailoring the side chain with the twisted oxygen-containing TPA group can increase the binding energy of O–Pb as well as enhance the electric field strength at the interface of FL02 and perovskite compared with the case of FL01, which favor both interfacial hole extraction and suppression of charge recombination as observed experimentally. As a result, the FL02 HTM-based n–i–p LHPSCs afford the highest PCE of 17.8%, significantly outperforming that (8.6%) of FL01-based ones, which is also comparable with the performance (18.8%) of Spiro-OMeTAD-based control devices. More importantly, due to the strong interfacial interaction between the twisted side chains of FL02 and perovskite surface, the diffusion of hygroscopic dopants in the HTM toward the perovskite can be effectively blocked or mitigated. This results in the enhanced stability of unencapsulated FL02-based devices with a long T_{80} lifetime of >98 h under continuous 1 sun illumination in air (RH = 40%) and a projected T_{80} lifetime of ≈270 days under the storage conditions (RH = 20%).

2. Results and Discussion

2.1. Design and Synthesis of FL01 and FL02 HTMs

Figure 1a shows the molecular structures of FL01 and FL02, which possess an identical D– π -D linear skeleton, except for different substituents on the side chains, i.e., PCZ group for FL01 and TPA group for FL02. From the structure point of view, the only molecular difference is that there is one C–C bond bridging between two end benzene rings on the side chain of FL01, which is absent in the case of FL02. The absence of this C–C bond allows the FL02 molecule to have high flexibility for forming the torsion on the side chain, as evident by the simulated large plane angles (>60°) among the three benzene rings in the TPA group, compared to those small values (<37°) in the case of PCZ group with high planarity (Figure 1b). Benefiting from the high space tolerance obtained from the twisted side chain, FL02 molecules are predicted to be more easily attached on the perovskite surface via the O–Pb bonding formed at the interface of HTM and perovskite, compared to the low possibility of interfacial O–Pb bond formation in the case of FL01/perovskite, owing

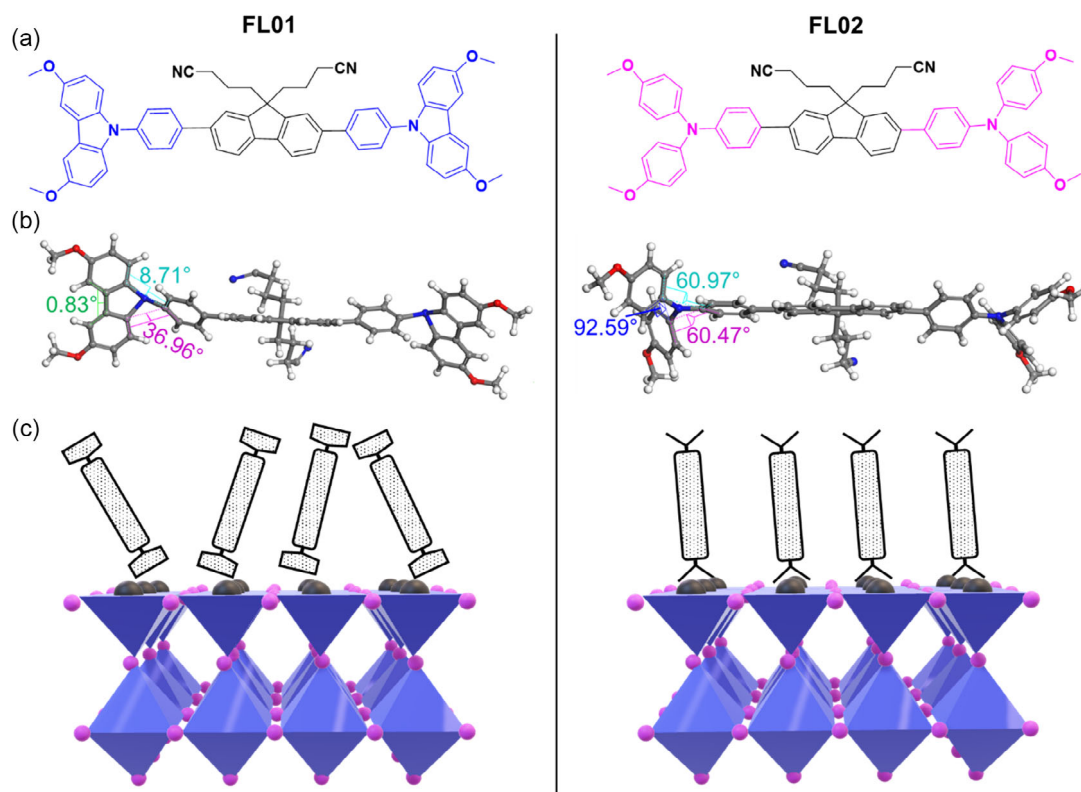


Figure 1. Molecular structures of a) FL01 (left) and FL02 (right). b) Optimized geometries of FL01 (left) and FL02 (right), presenting the plane angles among the three benzenes on the side chain. c) Hypothesized arrangements on the perovskite surface with PbX_2 terminal for FL01 (left) and FL02 (right) in a vertical orientation.

to the spatial blocking of conformational torsion by the highly planar side chain. The hypothesized arrangements for FL01 and FL02 vertically attaching on the perovskite surface with PbX_2 ($\text{X} = \text{Br}$ or I) terminal are presented in Figure 1c. FL01 and FL02 were synthesized through facile Suzuki coupling reaction in high yields ($>85\%$). The detailed synthetic routes of the two molecules are described in Scheme S1, Supporting Information, and their corresponding structural characterizations (Figure S1–S8, Supporting Information) verify the successful synthesis of target molecules. To investigate the thermal properties of as-synthesized FL01 and FL02 molecules, differential scanning calorimetry (DSC) analysis was conducted (Figure S9a,b, Supporting Information). FL02 shows a slightly higher glass transition temperature (T_g , $\approx 150^\circ\text{C}$) during the heating process compared to that ($\approx 142^\circ\text{C}$) of FL01 because both molecules tend to be amorphous as evident by the broad characteristic bands (17° – 34°) observed in the X-ray diffraction (XRD) patterns (Figure S9c, Supporting Information), suggesting that the twisted side chain plays a positive role in enhancing the thermal stability of this type of small molecules. It is also noted that there is no obvious exothermic peak (i.e., crystalline temperature, T_c) observed during the cooling process in both cases, demonstrating that FL01 and FL02 molecules are effectively amorphous materials. In addition, we measured the thermogravimetric analysis (TGA) for these two molecules (see Figure S9d, Supporting Information). Interestingly, FL01 and FL02 exhibit overall good thermal stability and no weight

loss was observed before 345°C , while a 5% weight loss similarly occurred at $>420^\circ\text{C}$ in both cases. The synthetic cost of FL02 is low with an estimated value of \$14.3 per gram (see the cost analysis in detail in Table S1–S5, Supporting Information), which is much lower than the commercially available HTMs, e.g., Spiro-OMeTAD (raw cost of \$91.7 per gram).^[13]

2.2. Optical, Electrochemical and Hole-Transport Properties

It is considered that the optical properties of small-molecule HTMs can be tuned by limiting the conjugation length upon the twisted molecular structure.^[21] Figure 2a,b depicts the UV–vis absorption spectra of FL01 and FL02 HTMs in their solution and solid states, respectively. The first exciton peaks ($\lambda_{\text{abs,exc}}$) of these two molecules are observed in the range of 358–407 nm, which are assigned to the partial charge transfer (CT) transition as observed for other type of fluorene-based small molecules.^[23] Interestingly, the FL02 molecule demonstrates a bathochromic shift of more than 20 nm compared to the case of FL01 both in solution and solid states, possibly due to the more favorable conformational twisting of FL02 in space, leading to a longer effective conjugation length between the fluorene core and adjacent benzene rings. The observed second exciton peaks in the range of 293–315 nm are attributed to the π – π^* electron transition of triphenylamine. Compared to the case in solution phase, both FL01 and FL02 films exhibit significantly redshifted

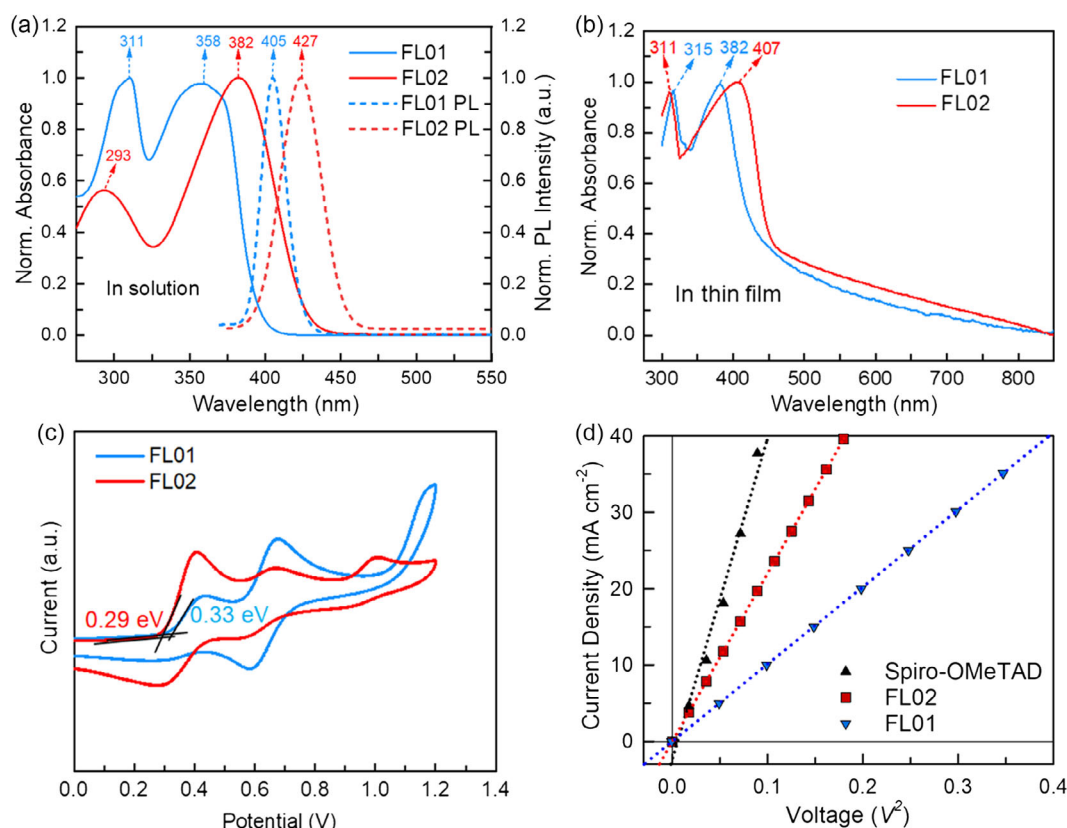


Figure 2. a) Steady-state absorption spectra and PL spectra of FL01 and FL02 in solution phase, and b) absorption spectra in film state. c) CV spectra of FL01 and FL02 solution in dichloromethane (DCM, 0.1 M) with the tetrabutylammonium hexafluorophosphate (TBAPF6, 0.1 M) as the supporting electrolyte. The oxidation potential was calculated versus ferrocene. d) Dark $J-V^2$ curves of FL01- and FL02-based hole-only devices in a configuration of 'ITO/PEDOT:PSS/HTM/MoO₃/Au'. The dotted line shows the fitting curve with a linear function.

(≈ 25 nm) spectra, suggesting that these two molecules possess similar aggregation behavior in film state. Moreover, the photoluminescence (PL) spectra of two molecules in solution phase were recorded upon the excitation at 360 nm, as compared in Figure 2a. A similar Stokes shift is observed for FL01 (≈ 47 nm) and FL02 (≈ 45 nm), respectively, confirming that a significant CT transition indeed contributes to the emission profile both in cases of FL01 and FL02. We then conducted the cyclic voltammetry (CV) measurements to determine the electrochemical properties of the two molecules (see the voltammograms in Figure 2c). The estimated highest occupied molecular orbital (HOMO) energy levels of FL01 and FL02 are -5.13 and -5.09 eV, respectively, according to the extracted oxidation onset potentials, which are deeper than that

(-5.04 eV) of conventional Spiro-OMeTAD measured under the identical conditions (see Figure S9e, Supporting Information). The deep HOMO energy levels of FL01 and FL02 can be attributed to the strong electron-withdrawing properties of the fluorene core and phenylamine moiety. The corresponding lowest unoccupied molecular orbital (LUMO) energy levels of FL01 and FL02 were calculated as -2.07 and -2.26 eV, respectively, based on the optical band gaps (E_g^{opt}) determined from the absorption spectra in solution phase. These values (summarized in Table 1) indicate that FL01 and FL02 exhibit suitable HOMO and LUMO energy levels for efficient charge transfer between perovskite and HTM, as evidenced by the performance of fabricated LHPSCs which will be discussed in the following Section 2.5.

Table 1. Optical, electrochemical, and hole transporting properties of FL01 and FL02 HTMs.

HTM	$\lambda_{\text{abs,exc}}$ [nm]		HOMO ^{a)} [eV]	LUMO ^{b)} [eV]	$E_g^{\text{opt(c)}}$ [eV]	$\mu_h^{\text{d)}}$ [cm ² V ⁻¹ s ⁻¹]
	Solution	Thin film				
FL01	358	382	-5.13	-2.07	3.06	9.8×10^{-5}
FL02	382	407	-5.09	-2.26	2.83	5.3×10^{-4}

^{a)}HOMO level was obtained by CV measurement: $-E_{\text{HOMO}} = E_{\text{onset(ox)}} + 4.8$ eV, where $E_{\text{onset(ox)}}$ is the onset potential for the oxidation versus ferrocene; ^{b)}LUMO level was obtained from the equation of $E_{\text{LUMO}} = E_{\text{HOMO}} + E_g^{\text{opt}}$; ^{c)}Optical bandgap E_g^{opt} was determined at the absorption onset of the molecule in solution phase ($E_g^{\text{opt}} = 1240/\lambda_{\text{abs,onset}}$ eV); ^{d)}Hole mobility.

The hole-transport properties of FL01 and FL02 HTMs were investigated by measuring their hole mobilities via the space-charge-limited current (SCLC) method. Figure 2d illustrates the comparison of dark $J-V^2$ curves of the various HTM-based hole-only devices for determining the hole mobilities (see the detailed method in the SI). The calculated hole mobility ($5.3 \times 10^{-4} \text{ cm}^2 \text{ V}^{-1} \text{ s}^{-1}$) of doped FL02 HTM is by a factor of >5 higher than that ($9.8 \times 10^{-5} \text{ cm}^2 \text{ V}^{-1} \text{ s}^{-1}$) of doped FL01 HTM (see Table 1), which is also comparable with that ($7.5 \times 10^{-4} \text{ cm}^2 \text{ V}^{-1} \text{ s}^{-1}$) of doped Spiro-OMeTAD HTM. This hints that the appropriate torsion on the side chain in addition to the planar core (FL02) can rather improve the intermolecular interaction, thus the hole mobility compared with purely planar FL01. This phenomenon has been similarly observed for other type of HTMs with the hybridized conformational structure.^[24]

2.3. Computed Interfacial Properties of Perovskite and HTMs

To gain insights into the interfacial properties of perovskite and HTMs, we conducted the DFT calculations (see the simulation

methods in detail in the Supporting Information) to simulate the adsorption states of FL01 and FL02 HTMs on the perovskite surface, by employing the $\text{CH}_3\text{NH}_3\text{PbI}_3$ (MAPbI_3) as the prototype of the CsFAMA (i.e., $\text{Cs}_{0.05}(\text{FA}_{0.83}\text{MA}_{0.17})_{0.95}\text{Pb}(\text{I}_{0.83}\text{Br}_{0.17})_3$) triple-cation halide perovskite in the actual device fabrication in this work. To probe the interaction between the oxygen atoms with electron lone pairs in HTMs and uncoordinated Pb^{2+} in perovskite, the PbI_2 -terminated (001) surfaces of perovskite slabs^[12] were used to model the formation of O—Pb bond at the interface. **Figure 3a,b** compares the optimized adsorption states of FL01 and FL02 HTMs vertically on the perovskite surface. Compared with FL01 with planar side chains, FL02 HTM with twisted side chains adsorbs more closer to the perovskite surface by showing shorter O—Pb bond lengths with the interaction angles of O—Pb—I more approaching 90° , indicating that the bond of O—Pb between FL02 and perovskite tends to be formed perpendicularly at the interface, which benefits from the high conformational flexibility of the twisted side chains (TPA groups). This leads to the highly enhanced adsorption binding energy ($-4.33 \text{ meV } \text{\AA}^{-2}$) between FL02 and perovskite compared

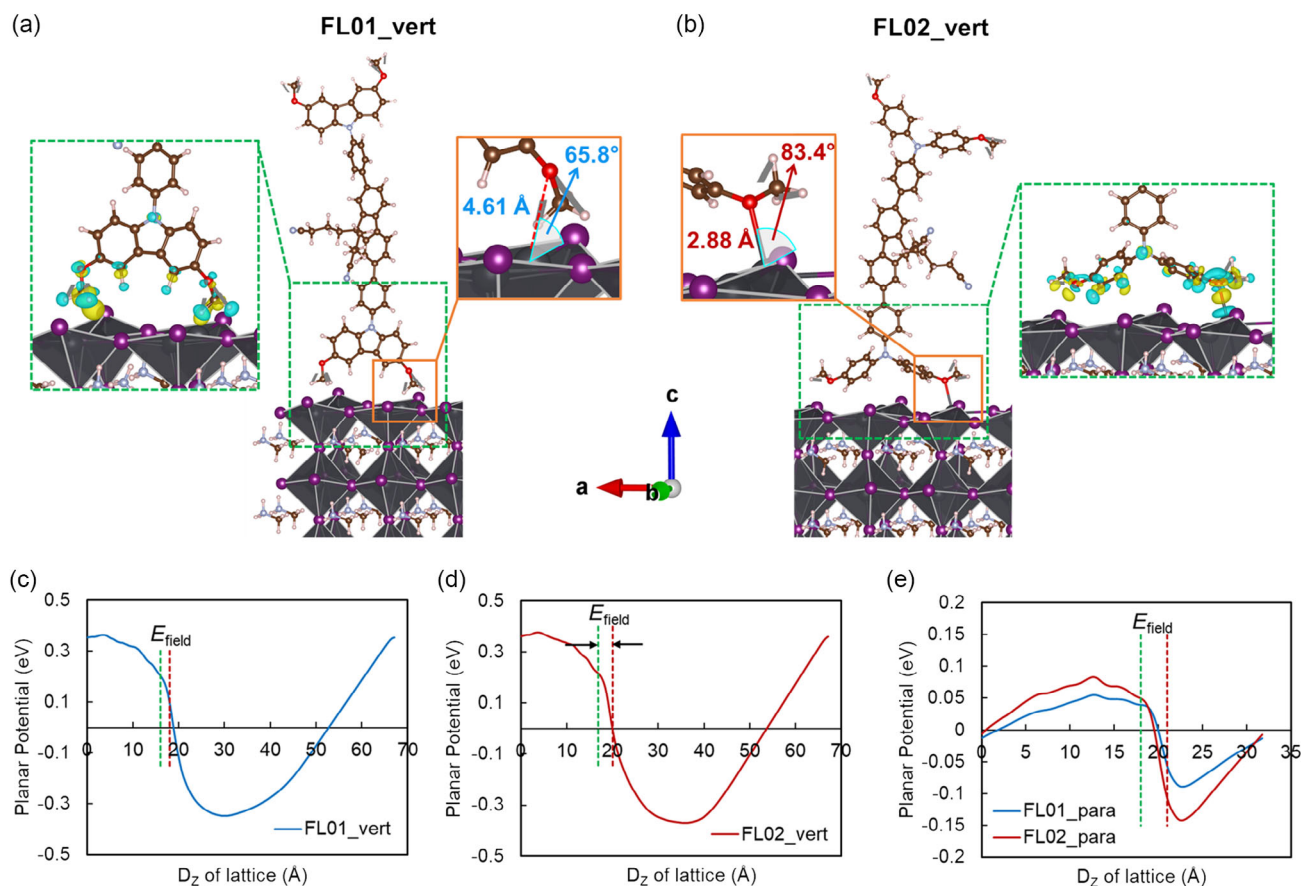


Figure 3. Optimized adsorption structures of a) FL01 and b) FL02 on the PbI_2 -terminated surface of MAPbI_3 perovskite in a vertical (vert) orientation, where the C, H, O, N, Pb, and I atoms are marked in brown, white, red, silver, black, and purple colors, respectively. Amplified orange solid boxes highlight the Pb—O bond lengths and the interaction angles of O—Pb—I. Amplified green dash boxes show the charge density differential plots of FL01 and FL02 at the interface of perovskite and HTM, where the charge depletion and accumulation regions are marked in cyan and yellow colors, respectively. Planar average potentials across the z-direction at the interfaces of c) perovskite/FL01_vert, d) perovskite/FL02_vert, and e) comparison of perovskite/FL01_para and perovskite/FL02_para in a parallel (para) orientation. The green and maroon dash lines show the approximate locations of perovskite and HTM surfaces at the interface, respectively.

with the case ($-1.80 \text{ meV } \text{\AA}^{-2}$) of FL01 HTM. A similar trend is also seen when the HTMs adsorb parallelly on the perovskite surface (see the case of parallel orientation in Figure S10, Supporting Information). We thus conclude that regardless of the adsorption orientation the twisted side chains in the FL02 HTM constantly favor the strong interaction at the HTM/perovskite interface (see the summarized simulation results in Table S6, Supporting Information). We then computed the differential charge density profiles of the two interfaces and the plots were drawn at the same isosurface value of 0.001. Considering these plots for the two HTM/perovskite interfaces (see the magnified green dash boxes in Figure 3a,b), FL02 HTM has the two charge regions, i.e., depletion and accumulation regions, which are localized almost equally throughout the TPA groups that are attached or closer to the perovskite surface. This is possibly attributed to the fact that the high spatial flexibility of the TPA groups initiates the parallel facing mode to the perovskite surface. In case of FL01 HTM, though both the charge density regions are distributed in the functional group (PCZ group), there is a clear observation of more localized regions closer to the FL01/perovskite interface, owing to the nonpossibility of torsion for the planar PCZ group toward the parallel attachment on the perovskite surface. When the HTMs parallelly adsorb on the perovskite surface (see the dash boxes in Figure S10, Supporting Information), the FL02 HTM shows that both the charge density regions are distributed almost equally throughout the molecule. However, for FL01 HTM, it is noted that the charge density regions are indeed distributed but still show a few localized high-density charge regions that are closer to the perovskite surface. This suggests that the extracted holes can be more easily delocalized at the FL02/perovskite interface compared with that of the case of FL01/perovskite, which is conducive to the hole extraction/transfer within the FL02 HTM.

To further understand the interfacial charge transfer, the intrinsic electric field was analyzed, which is supposed to be generated due to the charge redistribution during the formation of heterojunction at the perovskite/HTM interface. Figure 3c–e shows the planar average potentials across the z -direction of the simulated cells in the vertical and parallel orientations, respectively. The corresponding electric field generated at the interface is computed according to the formula $E_{\text{field}} = \frac{dV}{dz}$, where E_{field} is the electric field and dV is the potential difference between HTM and perovskite surfaces. In both cases (vertical and parallel HTM adsorption), the electric field strength is stronger at the perovskite/FL02 interface (Table S6, Supporting Information), indicating that the charge transport is more active in the case of FL02. It is noteworthy that the parallel mode of attachment to the perovskite surface is more favorable compared with the case of vertical mode. This is because, the vertical mode of either FL01 or FL02 HTM does not show the distinguishable potential difference between positive and negative charge regions, while the entire interface falls in positive potential region (for FL01) or on the boundary of positive and negative regions (for FL02). This hints that the interfacial charge transfer hardly occurs without the external bias application in the vertical mode. Overall, our simulation results provide the theoretical evidence that the twisted side chains in FL02 HTM are more beneficial for realizing the efficient interfacial charge transfer upon

the tailored interfacial properties compared with the case of FL01 HTM with the planar side chains.

2.4. Influence of Side-Chain Engineering of HTMs on Interfacial Charge Transfer

To evaluate the influence of the side-chain geometry of HTMs on the charge transfer process at the interface of perovskite and HTM, we first conducted steady-state PL measurements for three types of samples as glass/CsFAMA (control), glass/CsFAMA/FL01, and glass/CsFAMA/FL02. Figure 4a depicts the PL spectra of the three samples, which were excited at 600 nm to avoid exciting the residual PbI_2 with an exciton peak at $\approx 500 \text{ nm}$. A sharp PL peak at around 768 nm is observed for the control sample, owing to no occurrence of the expected charge transfer reaction in perovskite excited state. Both glass/CsFAMA/HTM samples demonstrate a distinguishable quench of the perovskite PL with a stronger quenching effect from the FL02 HTM. By comparing the PL amplitudes of the glass/CsFAMA/HTM samples with that of the glass/CsFAMA control sample, the quenching efficiency, also known as hole extraction efficiency, can be estimated, as summarized in Table 2. The FL02-based sample shows significantly enhanced hole extraction efficiency (95.8%) compared with that (77.0%) of the FL01-based one, indicating that the twisted side chains (TPA groups) in the FL02 HTM indeed favor the efficient hole extraction by forming the strong interfacial interaction as DFT simulated. To further investigate the interfacial charge transfer dynamics, we then monitored the time-resolved PL (TRPL) decays for the above three samples (Figure 4b). The glass/CsFAMA/FL02 sample exhibits an accelerated PL decay compared with the case of FL01 sample, hinting that the hole is extracted much faster at the interface of perovskite and FL02. As the PL decays for perovskite samples have been reported to behave nonexponentially when the excitation energy density is less than $\approx 10 \text{ } \mu\text{J cm}^{-2}$ ($\approx 2 \text{ } \mu\text{J cm}^{-2}$ in this work),^[25] we employed a kinetic analysis method, namely, one-dimension charge diffusion model (see the detailed explanation in the Supporting Information), to analyze the decays by extracting three charge transfer components, i.e., first-order trap-assisted recombination (k_1 as the rate constant), second-order nongeminate carrier recombination (k_2 as the rate constant), and hole extraction process (k_{HT} as the rate constant).^[26,27] As shown in Table 2, the hole extraction rate constant ($k_{\text{HT}} = 7.1 \times 10^8 \text{ s}^{-1}$) for FL02 HTM is almost one order of magnitude higher than that ($k_{\text{HT}} = 8.2 \times 10^7 \text{ s}^{-1}$) for FL01 HTM, which is mainly attributed to the retarded trap-assisted recombination as evident by the significantly reduced first-order rate constant ($k_1 = 2.1 \times 10^7 \text{ s}^{-1}$) for FL02 compared to that ($k_1 = 9.8 \times 10^7 \text{ s}^{-1}$) for FL01 HTM. This, in turn, reveals that the twisted side chains of FL02 HTM can more effectively passivate the perovskite surface defects acting as the recombination sites, which is also experimentally supported by the reduced hole trap density ($5.56 \times 10^{15} \text{ cm}^{-3}$) at the perovskite/FL02 interface compared with the case ($9.73 \times 10^{15} \text{ cm}^{-3}$) of FL01 HTM with planar side chains (see the calculation method and results (Figure S11, Supporting Information) for hole trap density in the Supporting Information).

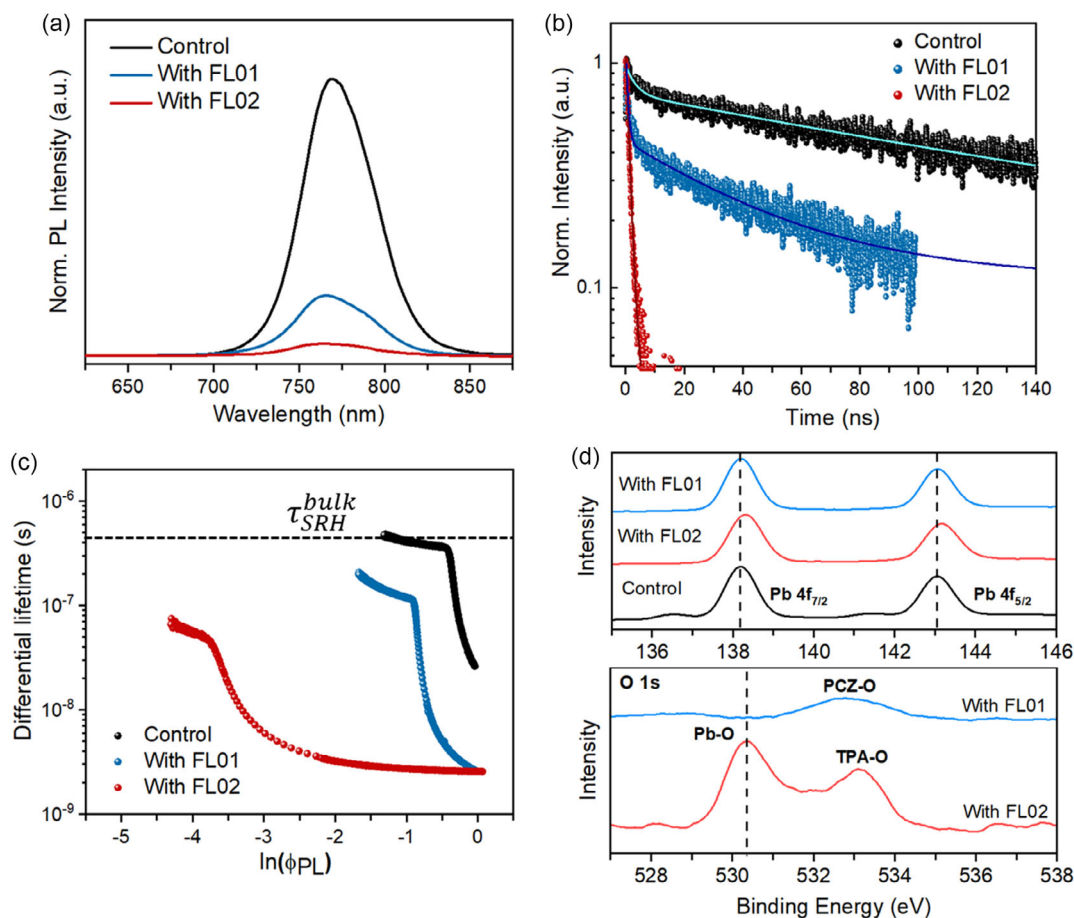


Figure 4. a) Steady-state PL spectra (excited at 600 nm), and b) TRPL decays (excited at 483 nm and monitored at PL peaks for each case) of pure perovskite film as control sample, perovskite/FL01 and perovskite/FL02 films. Solid lines in (b) represent the fitting results with a rate law equation. c) Differential lifetime (τ_{PL}) versus the logarithm of the TRPL intensity ($\ln(\phi_{PL})$). The plateau of τ_{PL} observed for the control sample was employed to estimate the SRH lifetime τ_{SRH}^{bulk} in the bulk. d) XPS spectra of perovskite films capped with and without HTMs for Pb (top) and O (bottom) elements.

Table 2. Interfacial charge transfer properties of perovskite/HTM interface.

HTM	ϕ_{HT} [%] ^{a)}	k_1 [s ⁻¹]	k_2 [s ⁻¹ cm ³]	k_{HT} [s ⁻¹]	τ_{PL} [ns] ^{b)}	S [cm s ⁻¹] ^{c)}	n_{trap} [cm ⁻³] ^{d)}
FL01	77.0	9.8×10^7	4.2×10^{-10}	8.2×10^7	119	665	9.73×10^{15}
FL02	95.8	2.1×10^7	4.0×10^{-10}	7.1×10^8	49	1814	5.56×10^{15}

^{a)}Hole extraction efficiency; ^{b)}Differential lifetime; ^{c)}Surface recombination velocity; ^{d)}Hole trap density.

As it is not easy to assess the lifetimes of one PL decay with three components, for simplicity, we thus used the term of differential lifetime (τ_{PL}) expressed in Equation (1)

$$\tau_{PL} = \left(-\frac{1}{m} \frac{d \ln(\phi_{PL})}{dt} \right)^{-1} \quad (1)$$

where $\phi_{PL}(t)$ is the PL intensity at a given time after the excitation and the m is a factor related to the extraction level, which is here defined as 2 by assuming that the CsFAMA perovskite is intrinsic.^[28–30] Figure 4c represents the results calculated based on Equation (1) by showing the differential lifetime versus logarithm of PL intensity ($\ln(\phi_{PL})$). The so-called effective

Shockley–Read–Hall (SRH) lifetime in the bulk, τ_{SRH}^{bulk} , can be extracted for the pure perovskite film (glass/CsFAMA) as 559.8 ns, which is consistent with reported for the same type of triple-cation perovskite.^[31] Consequently, by similarly extracting the effective SRH lifetimes (τ_{SRH}^{HTM}) during the hole extraction process (glass/CsFAMA/HTM), the surface recombination velocity (S) at the interface of perovskite and HTM can be estimated according to Equation (2)

$$\tau_{SRH}^{HTM} = \left(\frac{1}{\tau_{SRH}^{bulk}} + \frac{S}{2d} \right)^{-1} \quad (2)$$

where d is the thickness of perovskite layer. The surface recombination velocity of the glass/CsFAMA/FL02 sample shows almost 3 times higher than that of FL01-based one (Table 2), confirming the achievement of swift hole extraction and suppressed charge recombination, which is indeed favored by increasing the torsion of side chains in the case of FL02 HTM. We further verified the strong interfacial interaction via the formation of Pb—O bond at the interface of perovskite and FL02 HTM by conducting the X-ray photoelectron spectroscopy (XPS) analysis (Figure 4d). The O atoms-containing twisted side chains (TPA groups) in FL02 HTM demonstrate a strengthened interaction with Pb^{2+} ions on the perovskite surface compared with the case of planar FL01 HTM, which is highly consistent with the previously simulated stronger adsorption binding energy at the perovskite/FL02 interface. It is noteworthy that the effect of —CN groups at the core parts of two HTM molecules on the interaction with the surface of perovskite^[32] has been investigated by recording the XPS spectra of perovskite/HTM samples for nitrogen (N) element (Figure S12, Supporting Information). It is interesting to observe two characteristic peaks centered at 401.9 eV (C—N) and 400.3 eV (C=N)^[33] in both cases, respectively, which demonstrate almost equal impact on the interaction with the perovskite surface. We thus rule out the role of —CN groups both from the core parts of FL01 and FL02 HTMs in influencing the interfacial properties in this work.

2.5. Fabrication of FL HTMs-Based n-i-p LHPSCs

2.5.1. Device Performance

To evaluate the influence of side chain geometry of the FL HTMs on the photovoltaic performance, n-i-p triple-cation (CsFAMA) LHPSCs with an architecture of FTO/c-TiO₂/m-TiO₂/CsFAMA/HTM/Au were constructed (see the fabrication details in the Supporting Information). Based on the energy-level diagram of the standard devices (Figure 5a), both FL01 and FL02 HTMs are energetically suitable for the appropriate energy-level alignment with sufficient driving force for hole transport from the valence band of CsFAMA perovskite to the HOMO levels of HTMs. We first tuned the thickness of FL02 HTM by varying its precursor concentration in the range of 5–15 mg mL⁻¹ in chlorobenzene and the optimized thickness of ≈ 55 nm (see the cross-sectional scanning electron microscope (SEM) image in Figure 5b) upon the concentration of 10 mg mL⁻¹ was obtained to achieve the best performance (Table S7, Supporting Information), similar to the best case of FL01 HTM-based devices acquired upon the same concentration (10 mg mL⁻¹, Table S8, Supporting Information) of FL01 precursor. The thin FL02 HTM layer is almost one-third of that (≈ 160 nm) for the Spiro-OMeTAD layer as a control (see Figure S13, Supporting Information). This indicates that in addition to the raw material cost, the fabrication cost can also be significantly reduced with the FL02 HTM compared with the common Spiro-OMeTAD HTM while maintaining the high device performance. Figure 5c–f illustrates the statistical analysis (15 devices for each case) of the photovoltaic parameters for FL HTM-based LHPSCs comparing with the Spiro-OMeTAD HTM-based ones, which are summarized in Table 3. Surprisingly, when comparing FL01- and FL02-based devices, a remarkably

enhanced J_{sc} (23.2 mA cm⁻²) by 8 mA cm⁻², an improved FF (72.2%) by 13.6%, and a more than twice higher PCE (17.8%) are achieved for FL02 HTM-based LHPSCs, which is also very comparable with that (18.8%) of the Spiro-OMeTAD-based control devices. Compared with the case of FL01 HTM with planar side chains, we attribute the significant increase in the J_{sc} and FF to the twisted side chains of FL02 HTM-induced efficient hole extraction process and retarded nonradiative recombination at the perovskite/HTM interface, respectively, which are favored by the stronger O—Pb binding energy as well as by the reduced trap density on the perovskite surface.^[12,34] This is also evident from the comparison (Table 3) of the series (R_s) and shunt (R_{sh}) resistances extracted from the dark J - V characteristics (data are not shown here) of the devices. Upon the more effective interfacial functionalization of twisted side chains, the FL02-based devices exhibit lower R_s and higher R_{sh} which are around one-sixth and 3 times of the corresponding values in the case of FL01-based devices, respectively, contributing to the improved FF (72.2%) of FL02-based devices which is even higher than that (71.6%) of Spiro-OMeTAD-based ones.

Moreover, based on the comparison of J - V curves of champion LHPSCs (Figure 6a), a clear reduction in the hysteresis (Table 3) is observed for the FL02-based devices (H-index = 1.08) compared with that (H-index = 1.16) of the FL01-based ones, owing to both swift hole extraction at the perovskite/FL02 interface and high hole mobility within the FL02 HTM.^[31] The external quantum efficiency (EQE) spectra (Figure 6b) verify the dominance of the photocurrent generation by the interfacial charge extraction, i.e., hole extraction process, leading to the big gap of current density between FL01- and FL02-based devices as observed before. The integrated J_{sc} estimated from the EQE spectra exhibits $a < 5\%$ mismatch with the J_{sc} from the J - V curves in both cases, confirming the good agreement between the two experiments. The internal quantum efficiency (IQE) spectra (Figure S14, Supporting Information) were also recorded with the identical quantum system, which are consistent with the trend of the EQE profiles. It has been reported that the swift hole extraction process dominates the general charge separation efficiency (ϕ_{sep}) compared with the relatively slow electron extraction process in LHPSCs;^[25] therefore, the ϕ_{sep} can be assumed to be equal to the hole extraction efficiency (ϕ_{HT}) as illustrated in Table 2. We can estimate the overall charge collection efficiency (ϕ_{col}) according to the reported equation of $\phi_{col} = \frac{IQE}{\phi_{sep}} = \frac{IQE}{\phi_{HT}}$ ^[12,35] resulting in the highly improved ϕ_{col} of $\approx 85\%$ in FL02-based devices compared with that ($\approx 65\%$) of FL01-based ones. This further suggests that the twisted side chains of FL02 HTM can favor not only the interfacial charge separation but also the charge (hole) transport within the HTM.

2.5.2. Stability Study

The interfacial properties of perovskite and HTM play a key role in the device stability, particularly for the doped HTM (e.g., Spiro-OMeTAD) in n-i-p configuration, because the hygroscopic dopants (e.g., LiTFSI and tBP) in the HTM can gradually diffuse toward the perovskite and HTM interface, acting as a contact channel to introduce the adsorbed moisture for degrading the perovskite structure.^[31] To identify the effect of side-chain

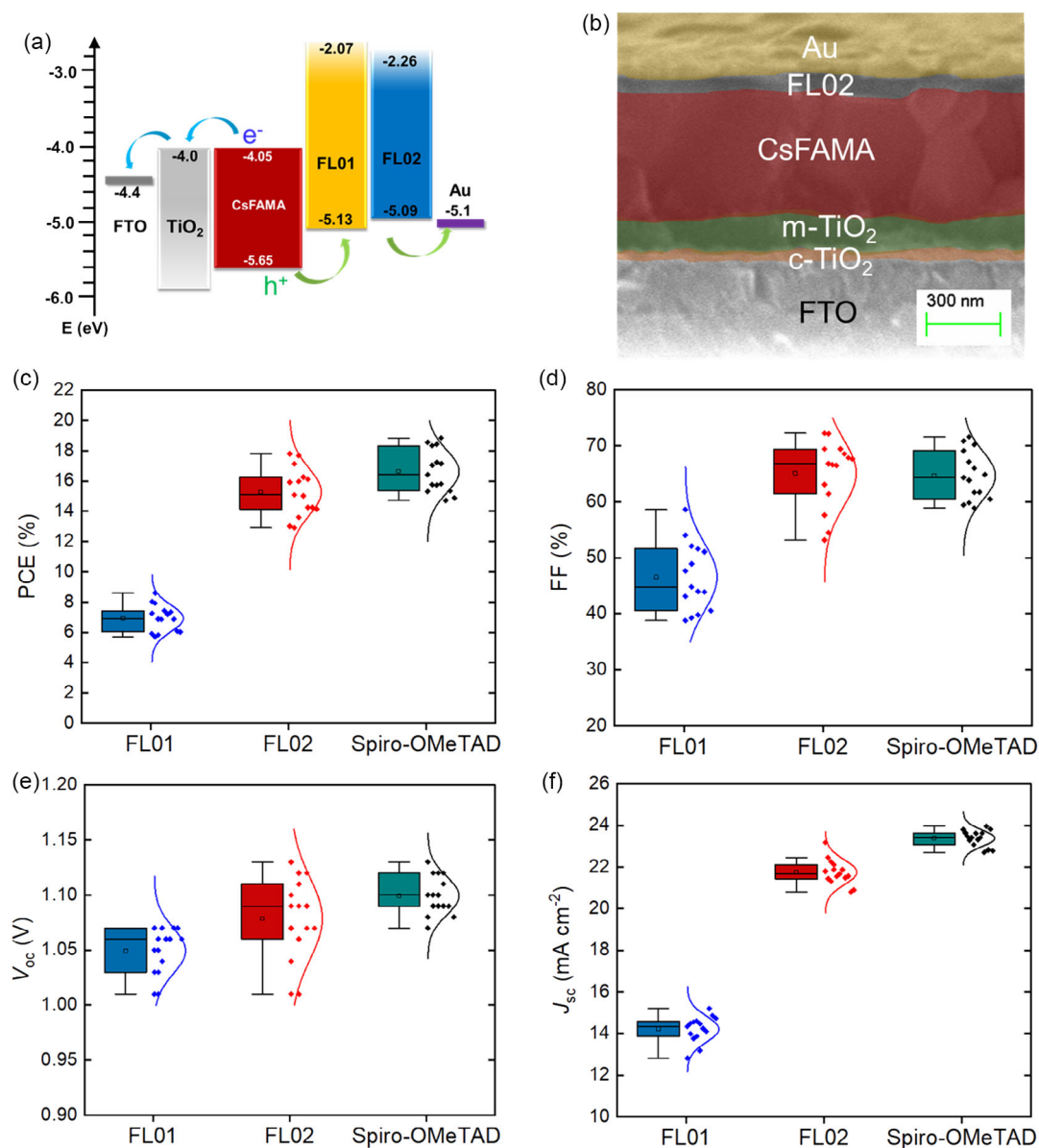


Figure 5. a) Energy-level diagram for each layer of the n-i-p LHPSCs. The HOMO energy level (data are not shown) of Spiro-OMeTAD is -5.04 eV versus vacuum, which was measured under the same cyclic voltammetric conditions as FL01 and FL02 HTMs. b) Cross-sectional SEM image of a typical FL02-based LHPSC with an estimated thickness of ≈ 55 nm for the FL02 layer. Photovoltaic parameters of c) PCE, d) FF, e) V_{oc} , and f) J_{sc} in box charts, obtained from 15 devices for each case.

Table 3. Performance of n-i-p LHPSCs fabricated with different HTMs. All data are recorded from the reverse scan.

HTM	PCE [%]	J_{sc} [mA cm^{-2}]	V_{oc} [V]	FF [%]	H-index ^{a)}	R_s [$\Omega \text{ cm}^2$]	R_{sh} [$\text{k}\Omega \text{ cm}^2$]
FL01	6.9 ± 0.9 (8.6) ^{b)}	14.2 ± 0.6 (15.2)	1.05 ± 0.02 (1.07)	46.5 ± 5.8 (58.6)	1.20 ± 0.03 (1.16)	32.2 ± 1.2 (29.4)	2.1 ± 0.4 (2.9)
FL02	15.3 ± 1.5 (17.8)	21.8 ± 0.6 (23.2)	1.08 ± 0.04 (1.13)	65.1 ± 5.8 (72.2)	1.11 ± 0.02 (1.08)	5.3 ± 0.4 (4.7)	6.2 ± 0.5 (7.0)
Spiro-OMeTAD	16.6 ± 1.4 (18.8)	23.4 ± 0.4 (23.9)	1.10 ± 0.02 (1.13)	64.7 ± 4.2 (71.6)	1.12 ± 0.03 (1.09)	6.9 ± 0.9 (5.6)	5.9 ± 0.4 (6.5)

^{a)} H-index is estimated as $\text{PCE}_{rev}/\text{PCE}_{for}$, where PCE_{rev} and PCE_{for} demonstrate the PCEs recorded under reverse and forward scans, respectively; ^{b)} The values in brackets correspond to the photovoltaic parameters of the champion cell.

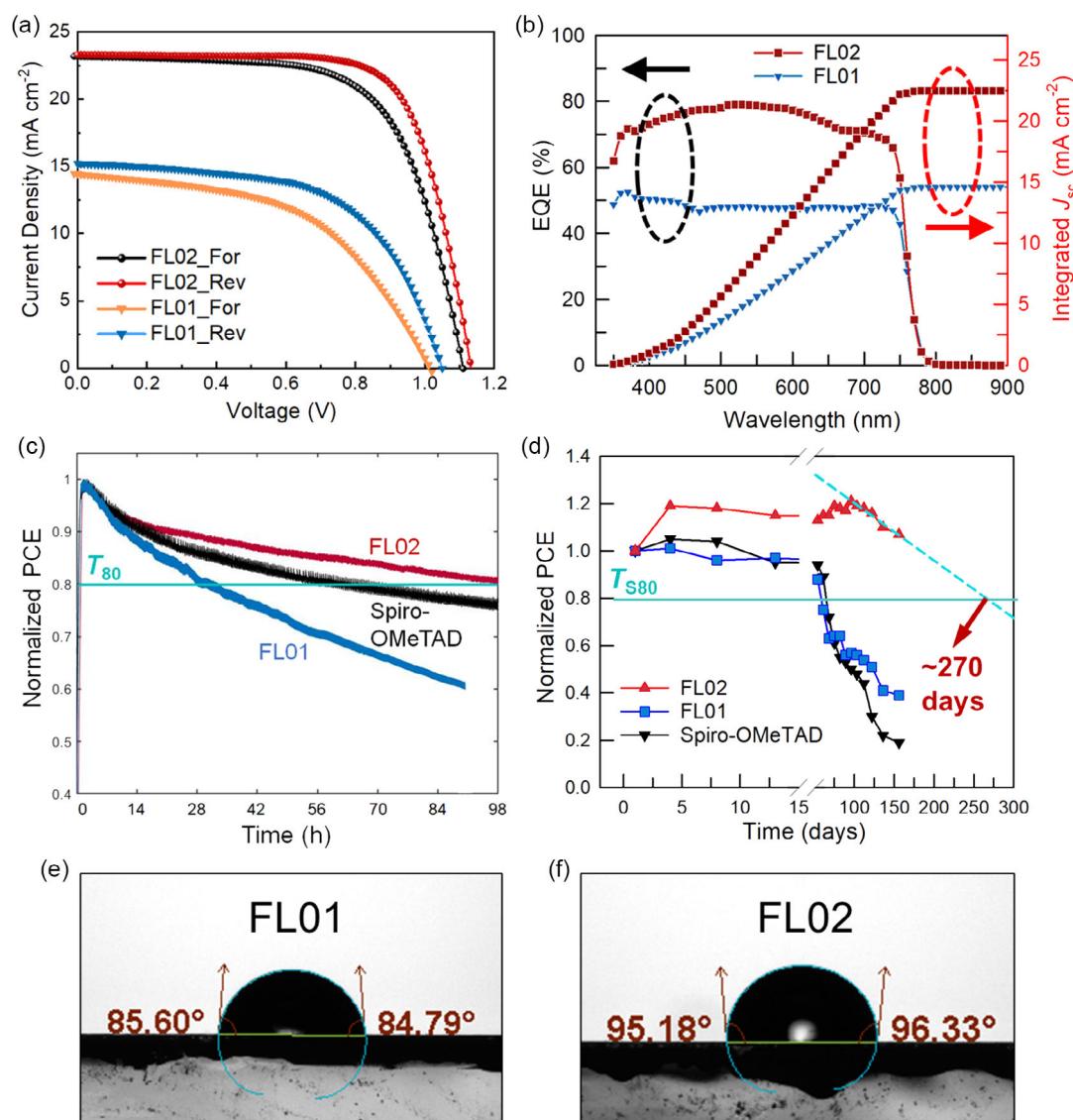


Figure 6. a) Current density (J)–voltage (V) curves of the champion FL01- and FL02-based LHPSCs under 1 sun condition (100 mW cm^{-2}), scanned from both forward and reverse directions with a scan rate of 50 mV s^{-1} . b) EQE spectra and corresponding integrated J_{sc} of the champion LHPSCs based on FL01 and FL02 HTMs. c) Normalized PCEs of the unencapsulated LHPSCs with different HTMs under the continuous 1 sun illumination in air (25°C and $\text{RH} = 40\%$). T_{80} demonstrates the time when the PCE decreases to 80% of its initial value upon the MPPT test. d) Normalized PCEs of the champion devices with various HTMs versus storage time, stored in a humidity-controlled cabinet (darkness, $\text{RH} = 20\%$) and measured in air. T_{80} represents the T_{80} lifetime of the devices in storage. Dash line shows the linear projection of the stability trend from the PCE peak point. Water contact angles (WCAs) for e) FL01 and f) FL02 coated on perovskite films.

engineering of HTMs on the operation stability of LHPSCs, the unencapsulated FL HTM- and Spiro-OMeTAD-based devices were measured in air ($\text{RH} = 40\%$) under continuous maximum power point tracking (MPPT) at 1 sun illumination and the normalized PCE tracks as a function of illumination time are demonstrated in Figure 6c. Compared with the FL01 (32 h)- and Spiro-OMeTAD (63 h)-based devices, the FL02-based cell features high operation stability with a longest T_{80} lifetime of $>98 \text{ h}$, which is much longer than the commonly reported T_{80} lifetimes ($<20 \text{ h}$) tested under the same conditions.^[36,37] Furthermore, we investigated the long-term stability by storing the devices in a relatively dry cabinet (darkness in air, $\text{RH} = 20\%$) and measuring

the periodic performance in ambient conditions ($\text{RH} = 40\%$), as shown in Figure 6d. Interestingly, the FL02-based cell exhibits a gradual increase in the PCE before 100 days of storage while both FL01- and Spiro-OMeTAD-based cells suffer a fast degradation right after around 50 days of storage. Upon the variation of photovoltaic parameters as a function of storage time (Figure S15, Supporting Information), it is clearly determined that the decrease in the J_{sc} dominates the decay of PCE in all cases, hinting that the effective protection of perovskite layer by the atop HTM is indeed crucial for realizing high stability of the n-i-p LHPSCs. We thus attribute the high operation and storage stabilities of FL02-based devices to two factors: 1) The surface

of FL02 HTM film shows a hydrophobic characteristic with a higher water contact angle (WCA) of 95° than 85° and 86° for the FL01 HTM and Spiro-OMeTAD HTM films (Figure 6e,f and S16, Supporting Information), respectively, ascribed to the lotus effect.^[38] 2) Compared with the weak and disordered interfacial interaction between the planar side chains (PCZ groups) of FL01 HTM and perovskite surface, the highly strong and oriented interaction via O—Pb bonding at the interface of twisted side chains (TPA groups) of FL02 HTM and perovskite can act as a barrier to block or mitigate the diffusion of hygroscopic dopants, i.e., LiTFSI, tBP, and cobalt complex (FK209) in this work, to penetrate into the perovskite layer by introducing the adsorbed water (moisture) and oxygen molecules, which significantly extends the lifespan of the devices.

3. Conclusions

In summary, we propose a simple yet effective strategy to synthesize a low-cost and well-balanced geometric HTM based on fluorene as the planar core, FL02, by tailoring the side chains with twisted TPA groups to efficiently functionalize the perovskite surface via the interaction of Pb—O bond. Our DFT simulations exhibit that the strong and oriented Pb—O bonds are formed at the perovskite and FL02 interface with strong electric field strength, due to the high conformational flexibility of the twisted side chains. Such optimum interfacial functionalization benefits the hole extraction process as well as the suppression of nonradiative recombination, which contribute to a significantly improved PCE (17.8%), being comparable with that (18.8%) of conventional Spiro-OMeTAD HTM-based devices. More importantly, both operation and storage stabilities of the FL02-based devices are dramatically enhanced by achieving T_{80} and T_{S80} lifetimes of >98 h and ≈270 days, respectively, mainly attributing to the effective blocking or mitigation of hygroscopic dopants diffusion toward the perovskite interface by a barrier-like intensive coordination of Pb—O bonding. Designing such a simple HTM with twisted side chains will afford better integration of efficient interfacial charge transfer and good protection on perovskite surface for obtaining high-performance and stable n-i-p LHPSCs.

Supporting Information

Supporting Information is available from the Wiley Online Library or from the author.

Acknowledgements

R.L. and M.L. contributed equally to this work. M.L. acknowledges the Finnish Cultural Foundation (grant no. 00220107) for the financial support. H.Z. thanks the support from Young Taishan Scholars under grant no. 201909120. P.V. acknowledges the financial support of Jane and Aatos Erkko foundation (SOL-TECH project), and Academy of Finland (decision no. 347772). J.T. acknowledges the 2022 Chinese national level of undergraduate on innovation and entrepreneurship training no. 202210426004. This work was partially supported by the Wallenberg Initiative Materials Science for Sustainability (WISE) funded by the Knut and Alice Wallenberg Foundation. This work is part of the Academy of Finland Flagship Programme, Photonics Research and Innovation (PREIN),

decision no. 320165. The computational review work was partly conducted with the support by JSPS KAKENHI grant no. JP22F32733, and partly with the support by the Australian government through the Australian Research Council (ARC) under the Centre of Excellence scheme (project no. CE170100026).

Conflict of Interest

The authors declare no conflict of interest.

Data Availability Statement

The data that support the findings of this study are available from the corresponding author upon reasonable request.

Keywords

computed interfacial electric field, hole-transport materials, interfacial charge transfer, n-i-p perovskite solar cells, twisted side chains

Received: June 2, 2023

Revised: July 3, 2023

Published online:

- [1] NREL, <https://www.nrel.gov/pv/cell-efficiency.html> (accessed: April 2023).
- [2] Ç. Odaş, Ö. Özer, R. Yıldırım, *Nano Energy* **2019**, *56*, 770.
- [3] W. S. Yang, B. W. Park, E. H. Jung, N. J. Jeon, Y. C. Kim, D. U. Lee, S. S. Shin, J. Seo, E. K. Kim, J. H. Noh, S. I. Seok, *Science* **2017**, *356*, 1376.
- [4] N. J. Jeon, H. Na, E. H. Jung, T. Y. Yang, Y. G. Lee, G. Kim, H. W. Shin, S. I. Seok, J. Lee, J. Seo, *Nat. Energy* **2018**, *3*, 682.
- [5] D. Luo, W. Yang, Z. Wang, A. Sadhanala, Q. Hu, R. Su, R. Shivanna, G. F. Trindade, J. F. Watts, Z. Xu, T. Liu, K. Chen, F. Ye, P. Wu, L. Zhao, J. Wu, Y. Tu, Y. Zhang, X. Yang, W. Zhang, R. H. Friend, Q. Gong, H. J. Snaith, R. Zhu, *Science* **2018**, *360*, 1442.
- [6] J. Peng, J. I. Khan, W. Liu, E. Ugur, T. Duong, Y. Wu, H. Shen, K. Wang, H. Dang, E. Aydin, X. Yang, Y. Wan, K. J. Weber, K. R. Catchpole, F. Laquai, S. De Wolf, T. P. White, *Adv. Energy Mater.* **2018**, *8*, 1801208.
- [7] R. Wang, J. Xue, K. L. Wang, Z. K. Wang, Y. Luo, D. Fenning, G. Xu, S. Nuryeva, T. Huang, Y. Zhao, J. L. Yang, J. Zhu, M. Wang, S. Tan, I. Yavuz, K. N. Houk, Y. Yang, *Science* **2019**, *366*, 1509.
- [8] J. Xie, K. Yan, H. Zhu, G. Li, H. Wang, H. Zhu, P. Hang, S. Zhao, W. Guo, D. Ye, L. Shao, X. Guan, T. Ngai, X. Yu, J. Xu, *Sci. Bull.* **2020**, *65*, 1726.
- [9] M. Saliba, S. Orlandi, T. Matsui, S. Aghazada, M. Cavazzini, J. P. Correa-Baena, P. Gao, R. Scopelliti, E. Mosconi, K. H. Dahmen, F. De Angelis, A. Abate, A. Hagfeldt, G. Pozzi, M. Graetzel, M. K. Nazeeruddin, *Nat. Energy* **2016**, *1*, 15017.
- [10] J. Zhang, B. Xu, L. Yang, C. Ruan, L. Wang, P. Liu, W. Zhang, N. Vlachopoulos, L. Kloo, G. Boschloo, L. Sun, A. Hagfeldt, E. M. J. Johansson, *Adv. Energy Mater.* **2018**, *8*, 1701209.
- [11] M. Li, J. Wu, G. Wang, B. Wu, Z. Sun, S. Xue, Q. Qiao, M. Liang, *J. Energy Chem.* **2020**, *47*, 10.
- [12] R. Li, M. Liu, S. K. Matta, A. Hiltunen, Z. Deng, C. Wang, Z. Dai, S. P. Russo, P. Vivo, H. Zhang, *Adv. Sustainable Syst.* **2021**, *5*, 2100244.
- [13] L. Canil, J. Salunke, Q. Wang, M. Liu, H. Köbler, M. Flatken, L. Gregori, D. Meggiolaro, D. Ricciarelli, F. De Angelis,

- M. Stolterfoht, D. Neher, A. Priimagi, P. Vivo, A. Abate, *Adv. Energy Mater.* **2021**, *11*, 2101553.
- [14] C. Wang, M. Liu, S. Rahman, H. P. Pasanen, J. Tian, J. Li, Z. Deng, H. Zhang, P. Vivo, *Nano Energy* **2022**, *101*, 107604.
- [15] K. Yang, Q. Liao, J. Huang, Z. Zhang, M. Su, Z. Chen, Z. Wu, D. Wang, Z. Lai, H. Y. Woo, Y. Cao, P. Gao, X. Guo, *Angew. Chem.* **2022**, *134*, 202113749.
- [16] A. Farokhi, H. Shahroosvand, G. D. Monache, M. Pilkington, M. K. Nazeeruddin, *Chem. Soc. Rev.* **2022**, *51*, 5974.
- [17] T. Niu, W. Zhu, Y. Zhang, Q. Xue, X. Jiao, Z. Wang, Y. M. Xie, P. Li, R. Chen, F. Huang, Y. Li, H. L. Yip, Y. Cao, *Joule* **2021**, *5*, 249.
- [18] Y. Wang, Q. Chen, J. Fu, Z. Liu, Z. Sun, S. Zhang, Y. Zhu, X. Jia, J. Zhang, N. Yuan, Y. Zhou, B. Song, Y. Li, *Chem. Eng. J.* **2022**, *433*, 133265.
- [19] X. Yu, Z. Li, X. Sun, C. Zhong, Z. Zhu, Z. Li, A. K. Y. Jen, *Nano Energy* **2021**, *82*, 105701.
- [20] Y.-D. Lin, B.-Y. Ke, K.-M. Lee, S. H. Chang, K.-H. Wang, S.-H. Huang, C.-G. Wu, P.-T. Chou, S. Jhulki, J. N. Moorthy, Y. J. Chang, K.-L. Liao, H.-C. Chung, C.-Y. Liu, S.-S. Sun, T. J. Chow, *ChemSusChem* **2016**, *9*, 274.
- [21] X. Yang, J. Xi, Y. Sun, Y. Zhang, G. Zhou, W. Y. Wong, *Nano Energy* **2019**, *64*, 103946.
- [22] R. Wang, T. Li, C. Liu, M. Xie, H. Zhou, Q. Sun, B. Yang, S. T. Zhang, S. Xue, W. Yang, *Adv. Funct. Mater.* **2022**, *32*, 2201143.
- [23] A.-L. Capodilupo, F. Manni, G. A. Corrente, G. Accorsi, E. Fabiano, A. Cardone, R. Giannuzzi, A. Beneduci, G. Gigli, *Dye. Pigm.* **2020**, *177*, 108325.
- [24] C. Shen, Y. Wu, H. Zhang, E. Li, W. Zhang, X. Xu, W. Wu, H. Tian, W. Zhu, *Angew. Chem. Int. Ed.* **2019**, *58*, 3784.
- [25] S. Makuta, M. Liu, M. Endo, H. Nishimura, A. Wakamiya, Y. Tachibana, *Chem. Commun.* **2016**, *52*, 673.
- [26] M. Liu, M. Endo, A. Shimazaki, A. Wakamiya, Y. Tachibana, *J. Photopolym. Sci. Technol.* **2018**, *31*, 633.
- [27] M. Liu, M. Endo, A. Shimazaki, A. Wakamiya, Y. Tachibana, *ACS Appl. Energy Mater.* **2018**, *1*, 3722.
- [28] B. Krogmeier, F. Staub, D. Grabowski, U. Rau, T. Kirchartz, *Sustainable Energy Fuels* **2018**, *2*, 1027.
- [29] T. Kirchartz, J. A. Márquez, M. Stolterfoht, T. Unold, *Adv. Energy Mater.* **2020**, *10*, 1904134.
- [30] L. Krückemeier, B. Krogmeier, Z. Liu, U. Rau, T. Kirchartz, *Adv. Energy Mater.* **2021**, *11*, 2003489.
- [31] M. Liu, S. Dahlström, C. Ahläng, S. Wilken, A. Degterev, A. Matuhina, M. Hadadian, M. Markkanen, K. Aitola, A. Kamppinen, J. Deska, O. Mangs, M. Nyman, P. D. Lund, J.-H. Smätt, R. Österbacka, P. Vivo, *J. Mater. Chem. A* **2022**, *10*, 11721.
- [32] S. Daskeviciute-Geguziene, Y. Zhang, K. Rakstys, C. Xiao, J. Xia, Z. Qiu, M. Daskeviciene, T. Paskevicius, V. Jankauskas, A. M. Asiri, V. Getautis, M. K. Nazeeruddin, *Adv. Funct. Mater.* **2023**, *33*, 2208317.
- [33] M. C. Tang, S. Zhang, T. J. Magnanelli, N. V. Nguyen, E. J. Heilweil, T. D. Anthopoulos, C. A. Hacker, *Mater. Adv.* **2021**, *2*, 1253.
- [34] L. M. Herz, *Annu. Rev. Phys. Chem.* **2016**, *67*, 65.
- [35] M. Liu, M. Endo, A. Shimazaki, A. Wakamiya, Y. Tachibana, *J. Photopolym. Sci. Technol.* **2017**, *30*, 577.
- [36] N. Li, X. Niu, Q. Chen, H. Zhou, *Chem. Soc. Rev.* **2020**, *49*, 8235.
- [37] S. Zhang, Z. Liu, W. Zhang, Z. Jiang, W. Chen, R. Chen, Y. Huang, Z. Yang, Y. Zhang, L. Han, W. Chen, *Adv. Energy Mater.* **2020**, *10*, 2001610.
- [38] N. Cai, F. Li, Y. Chen, R. Luo, T. Hu, F. Lin, S. Yiu, D. Liu, D. Lei, Z. Zhu, A. K. Y. Jen, *Angew. Chem. Int. Ed.* **2021**, *60*, 20437.